Materials & Design 260 (2025) 115029

Contents lists available at ScienceDirect

Materials & Design

journal homepage: www.elsevier.com/locate/matdes

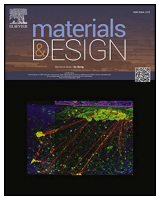

Microstructural evolution and mechanical behavior of friction stir welded additively manufactured Haynes 282 Ni superalloy

Abhishek Sharma [a,*], Sukhdeep Singh [b,c], Yoshiaki Morisada [a], Kohsaku Ushioda [a], Joel Andersson [b], Hidetoshi Fujii [a,*]

[a] Joining & Welding Research Institute, The University of Osaka, Osaka 567-0047, Japan
[b] Department of Engineering Science, University West, Trollhättan SE-46186, Sweden
[c] Research & Development, NKT HV Cables AB, Karlskrona SE-37123, Sweden

ARTICLE INFO

Keywords:
Friction stir welding (FSW)
Haynes 282
Ni superalloy
Additive manufacturing
Electron beam powder bed fusion (EB-PBF)

ABSTRACT

Haynes 282 (H282) is a gamma prime (γ′) strengthened nickel-based superalloy with applications in jet engine turbine components and other aerospace applications. Electron beam powder bed fusion (EB-PBF) additive manufacturing (AM) enables efficient fabrication of H282 by promoting in-situ γ′ precipitation. However, integrating AMed parts with conventionally made components is cost-effective and often necessary, requiring reliable joining methods. This study explores friction stir welding (FSW) of as-built EB-PBF H282 using a novel hemispherical Si_3N_4 tool tilted toward the retreating side. A joint efficiency of 100 % in ultimate tensile strength was achieved in both as-welded and post-weld heat-treated (PWHT) conditions. UTS increased from ~ 1000 MPa (as-built) to ~ 1039 MPa after FSW, and ~ 1258 MPa after PWHT. FSW induced dynamic recrystallization, refining grain size from ~ 170 μm to ~ 7 μm in the stir zone, while also eliminating typical AM defects like porosity and lack of fusion. During FSW, γ′ precipitates dissolved in the SZ but were restored during PWHT along with other strengthening phases—Ti-, Mo-rich MC, and Cr-rich $M_{23}C_6$ carbides. The main strengthening mechanisms were Hall-Petch, dislocation, and precipitation strengthening. Results are compared to FSW of solution-annealed AM H282 and wrought H282, confirming FSW's effectiveness in enhancing microstructural and mechanical performance.

1. Introduction

Haynes 282 (H282) is a γ′-strengthened nickel-based superalloy designed for the production of hot-section components in gas turbines used in aircraft engines and power plants [1]. It is also considered a promising material for rotor, blade, and exhaust casing components in the next generation of advanced ultra-supercritical power plants, capable of withstanding operating temperatures up to 760 °C and pressures up to 31 MPa [2]. The alloy's high-temperature strength is primarily due to the presence of $L1_2$ γ′ precipitates and carbides. H282's superior tensile and creep properties, compared to other typical nickel-based superalloys such as Waspaloy and Rene-41, are attributed mainly to its controlled and relatively low fraction of γ′ phase [3]. This phenomenon not only reduces strain-age cracking and liquation cracking but also enhances the alloy's fabricability and weldability, making it suitable for fabrication via additive manufacturing [4].

Additive manufacturing (AM) is a technique of producing three-dimensional parts through layer-by-layer deposition of metallic material. The AM techniques have gained quick popularity in the last few years due to the ease of fabricating complex components, along with increased performance and structural optimization. In recent years, the H282 alloy was also successfully processed by various researchers through different AM techniques, such as direct energy deposition by laser (DED-L) [5], wire arc additive manufacturing (WAAM) [6], laser powder bed fusion (L-PBF) [7], and electron beam powder bed fusion (EB-PBF) [8]. The relatively low residual stresses, reduced cracking tendency, and in-situ formation of γ′ precipitates associated with the EB-PBF make it a particularly promising method for printing H282 alloy components [9].

The AMed parts are more expensive than castings when produced in large quantities due to higher upfront tooling costs and material costs per part [10]. However, AM can be more cost-effective for small runs of custom parts because of its design flexibility and ability to create complex geometries without requiring extensive tooling. As a result, AM is

* Corresponding authors.
E-mail addresses: sharma.abhishek.jwri@osaka-u.ac.jp (A. Sharma), fujii.hidetoshi.jwri@osaka-u.ac.jp (H. Fujii).

https://doi.org/10.1016/j.matdes.2025.115029
Received 26 August 2025; Received in revised form 9 October 2025; Accepted 24 October 2025
Available online 25 October 2025

typically advantageous for producing intricate components that are then assembled through welding to make the final product. Additionally, welding is extensively practical for repairing and remanufacturing service-damaged AMed and cast components, particularly in applications such as turbine engines [11,12], where extreme environments make the component more susceptible to cracking [13]. Since additively manufactured components are expensive and feature complex geometries, repair and remanufacturing are often more important than outright replacement.

The annealed H282 alloy generally exhibits good weldability for a γ′-strengthened alloy, with satisfactory resistance to strain-age cracking [14]. However, fusion welding techniques, such as laser beam welding, often result in microsegregation and non-equilibrium phase transformations in the welds during solidification [15]. Dendritic microsegregation leads to the formation of intermetallic secondary solidification phases along the dendrite boundaries and an uneven distribution of secondary phase precipitates. In some cases, strengthening carbides (such as MC, M_6C, and $M_{23}C_6$) also segregate in the interdendritic regions, which can degrade the material's performance at elevated temperatures [5]. Additionally, grain boundary liquation and cracking in the heat-affected zone (HAZ) of H282 alloy have been reported by several researchers [16,17].

Friction stir welding (FSW) is a solid-state joining technique that can potentially address the challenges of joining H282 alloy [18]. However, the high strength of Ni-base superalloys at the elevated welding temperatures in FSW leads to accelerated tool wear and often causes probe fractures [19]. The probe, being the most delicate part of the FSW tool, is particularly vulnerable due to the higher stress concentration on its reduced cross-section. In the absence of material softening, the increased resistance to linear motion of the tool contributes to probe fractures during the FSW of H282 alloy. The first study on FSW of H282 alloy was conducted by Komarasamy et al. [20], where the authors successfully joined wrought H282 alloy using an expensive polycrystalline cubic boron nitride (PCBN) tool, achieving 100 % joint efficiency compared to the base material. Interestingly, the creep-rupture lifetime of the joint was similar to that of the base metal [21]. More recently, in our previous study [22], we have demonstrated using a novel hemispherical dome-shaped tool of silicon nitride (Si_3N_4), tilted towards the retreating side (RS), to join wrought H282 alloy with 100 % joint efficiency. Here, Si_3N_4 is chosen as the tool material due to its excellent fracture toughness at high temperatures [23]. Additionally, Si_3N_4 remains stable at elevated welding temperatures and is more cost-effective than PCBN tools. In a subsequent study [24], the FSW processing parameters were optimized at various welding speeds (30, 100, and 200 mm/min). Notably, the joint strength of the wrought H282 alloy remained largely unaffected by variations in heat input, highlighting a key advantage of FSW over conventional fusion welding techniques, which require stringent control of process parameters.

The studies mentioned above on FSW of H282 alloy focus on the wrought form of the alloy in a solution-annealed state, followed by post-weld heat treatment (PWHT). In contrast, the EB-PBF AMed alloy is in a precipitation-hardened state and has a coarse-grained microstructure. As a result, its strength and hardness in the as-built condition are significantly higher than those of the wrought alloy. These variations in strength and hardness of the base material substantially influence heat generation through frictional interaction and plastic deformation. Consequently, the material flow behavior within the weld zone changes, affecting the alloy's overall weldability. Therefore, the welding parameters optimized for the wrought alloy cannot be directly applied to the AMed alloy; instead, a detailed investigation is necessary to successfully assess the weldability of the AMed alloy. This makes it particularly interesting to evaluate the weldability of AMed H282 alloy in terms of joint strength and microstructural evolution. In this study, we also performed FSW on the AMed alloy after solution heat treatment. The solution annealing of the EB-PBF manufactured H282 alloy led to precipitate dissolution, resulting in reduced hardness. Finally, the joint strength of the EB-PBF and solution-annealed states is compared to that of the wrought H282 alloy. This comparison establishes a fundamental understanding of the variation in the weldability of H282 alloy made of different processing pathways i.e. wrought and AMed.

2. Materials & methods

2.1. Starting materials

In this study, the base materials for FSW are as-built EB-PBF AMed H282 alloy, its solution annealed one and wrought H282 alloy of dimensions 110 (l) × 60 (w) × 3.5 (t) mm. Table 1 presents the notations used to refer to the base materials (sometimes referred to as starting materials), FSWed joints, and PWHT specimens throughout the paper. Table 2 represents the chemical composition of AM and W-H282 specimens. The detailed process parameters and manufacturing of AM plates by EB-PBF are reported elsewhere [8]. In the SAAM specimen, the AM specimen is subjected to solution annealing at 1135 °C for 2 hrs to dissove in-situ precipitated γ′ during the EB-PBF, followed by water quenching. Therefore, the starting materials (Haynes 282) for FSW in the present study are: AM, SAAM, and W-H282.

2.2. Friction stir welding and post-weld heat treatment

Friction stir welding was performed on the starting materials in a "bead-on-plate" configuration using a dedicated FSW setup under position-controlled settings. A hemispherical dome-shaped tool made of Si_3N_4 with a 7.5 mm dome radius was used for welding. The key process parameters for FSW are selected based on our previous studies and includes a tool rotational rate of 400 rpm, a welding speed of 30 mm/min, a tool tilt angle of 7° towards the retreating side (RS), and a plunge depth of 3 mm [22]. The axial force during welding was monitored using in-built load cells within the FSW setup. Welding temperature measurements were taken using an infrared thermal camera (FLIR) and a K-type thermocouple positioned at the surface on the weld centerline. The schematic representation of the experimental setup and sample scheme is illustrated in Fig. 1.

A two-step PWHT (see Fig. 1) was performed on the joints after FSW following the conditions recommended by Haynes International: (i) aging at 1010 °C for 2 h, followed by air cooling (AC), and (ii) aging at 788 °C for 8 h, followed by AC.

2.3. Microstructural characterization and mechanical testing

The tensile and microstructural characterization specimens were obtained perpendicular to the welding direction using wire electric discharge machining (EDM). The weld bead profile was measured using an optical surface profilometer (Keyence, VR320). The specimens for microstructural observation were progressively polished with abrasive paper (240 to 4000 grit) and subsequently buff-polished using a 1 μm

Table 1
Specimen notations.

Notation	Description
AM	As- Additively manufactured (in-situ precipitation strengthened) H282 Alloy
SAAM	AM + Solution annealing at 1135 °C for 2 hrs
W-H282	Wrought Haynes 282 alloys (soft annealed)
AM-FSW	AM + FSW
SAAM-FSW	SAAM + FSW
W-H282-FSW	W-H282-FSW
AM − PWHT	AM-FSW + PWHT*
SAAM − PWHT	SAAM-FSW + PWHT*
W-H282 − PWHT	W-H282-FSW + PWHT*

*PWHT refers to the two-step ageing heat treatment: (Step 1) 1010 °C for 2 hrs followed by air cooling, and (Step 2) 788 °C for 8 hrs followed by air cooling.

Table 2
Elemental composition of AMed and W-H282 base materials (wt.%).

	Ni	Cr	Co	Mo	Ti	Al	Mn	Fe	Si	C
W-H282	Bal.	19.49	10.36	8.55	2.16	1.52	0.05	0.37	0.05	0.072
AM	Bal.	19.1	10.2	8.5	2.08	1.63	< 0.1	< 0.1	0.02	0.05

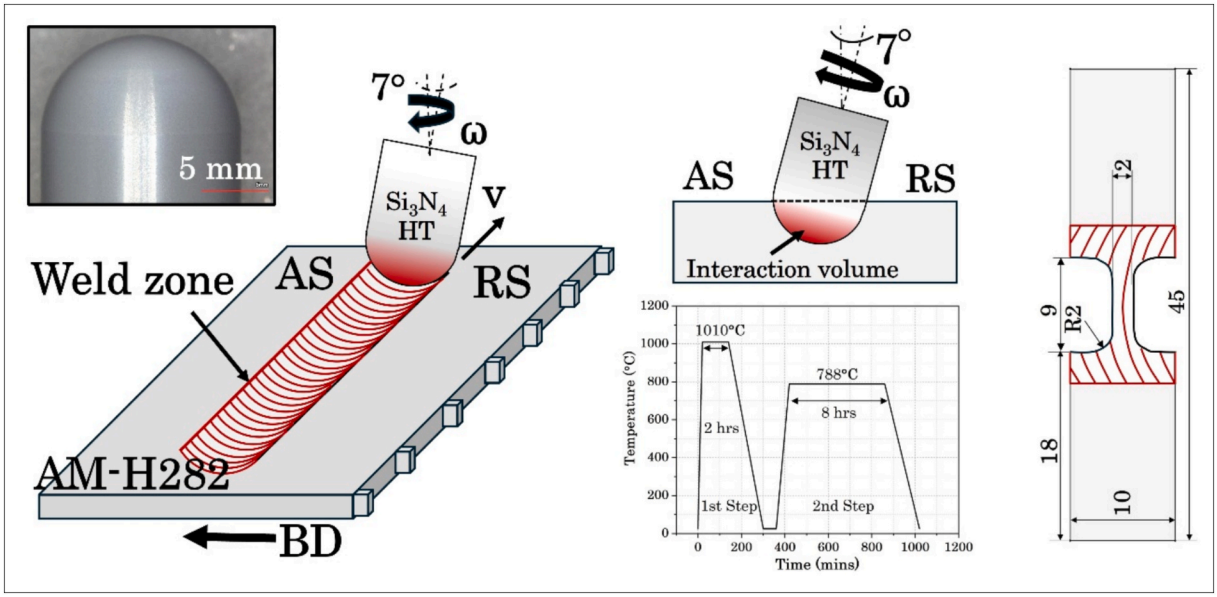

Fig. 1. Schematic representation of FSW process, specimen scheme, and PWHT cycle.

diamond suspension. Lastly, electropolishing was conducted in a solution of ethanol, 2-butoxyethanol, and perchloric acid at 16 V for 8 s. The microstructural evolution and constituent phases in the welded zone were examined using a field emission scanning electron microscope (FE-SEM, JEOL JSM-7001FA) equipped with energy-dispersive spectroscopy (EDS) and electron backscattered diffraction (EBSD) attachments. The EBSD scans were performed with a step size of 0.2 μm. The thin foil specimens for transmission electron microscopy (TEM, JEOL 2100F) analysis were obtained from the SEM specimens' cross-sectional surface using a focused ion beam milling (FIB, Hitachi FB-2000S).

The tensile specimen design ensured that the 5 mm gauge length encompassed the SZ allowing for an accurate evaluation of the weld zone's actual tensile strength. The specimens were ground to approximately 0.5 mm on the FSW surface and 1 mm from the bottom side, resulting in a final thickness of 2 mm, corresponding to the effective plunge depth. Room temperature tensile testing was performed using an Instron Universal Testing Machine at a 0.6 mm/min loading speed. Strain during tensile loading was measured through digital image correlation (DIC) following a previously reported method [25]. Microhardness mapping examination was conducted using a Vickers microhardness tester (Future Tech, FM-800) under a load of 100 kgf, with a dwell time of 15 s and a pitch of 0.25 mm on both x and y axes.

3. Results

3.1. Starting material microstructure

Fig. 2 (a-c) presents the SEM micrographs of the starting materials: AM, SAAM, and W-H282, respectively. The as-built EB-PBF process resulted in the in-situ precipitation of fine γ′ phase, which is visible in Fig. 2(a). The microstructure also contains Mo- and Ti-rich MC carbides, as indicated by the encircled region. EDS analysis, shown in Table 3, confirmed the elemental composition of these carbide phases. Fig. 2(b) illustrates the dissolution of the γ′ phase during solution annealing in the SAAM specimen. However, the high-temperature exposure also led to the formation of oxides, as seen by the bright particles in Fig. 2(b). Interestingly, the as-built AM and SAAM specimens also show the presence of gas pores and a lack of fusion defects, as shown in Fig. 1s (supplementary information). These defect are the preferenatial sites for the elemental segregation as shown through EDS mapping in Figs. 2s and 3s (supplementary information). The microstructure of the W-H282 specimen consists of intergranular interconnected carbide phases, as shown in Fig. 2(c), with the carbides identified as Ti- and Mo-rich primary MC carbides. Therefore, the three starting materials exhibit distinctly different microstructures and mechanical properties, making them ideal for comparing the FSW behavior of the alloy.

Fig. 2(d-f) displays the EBSD inverse pole figure (IPF) maps of the starting materials, along with the average grain size shown in Fig. 2(g). The as-built AM exhibits a coarse-grained microstructure, with an average grain size of approximately 170 μm. Solution annealing at high temperature in the SAAM specimen further coarsened the grains to an average size of around 220 μm. Interestingly, the AM and SAAM specimens show elongated grains with no evidence of twin boundaries. In contrast, the plastic deformation and work hardening in the wrought W-H282 specimen (Fig. 2(f)) resulted in a fine-grained structure of approximately 48 μm, with large twin structures present.

3.2. Temperature, axial force during FSW, and weld bead profile

Fig. 3(a) illustrates the maximum temperature profile recorded at the tool-substrate interface during welding. Notably, the maximum temperature remains around 1050 °C throughout the welding process for all three states of H282 alloy (AM, SAAM, and W-H282). The temperature measurements obtained using infrared thermal imaging and thermocouples are in perfect agreement. The welding temperature exceeds the γ′ solvus temperature (~ 997 °C) in the austenitic γ matrix, which causes the in-situ precipitated γ′ phase in the AM specimen to dissolve within the weld zone [1]. As a result, all three alloy states exhibit a weld zone

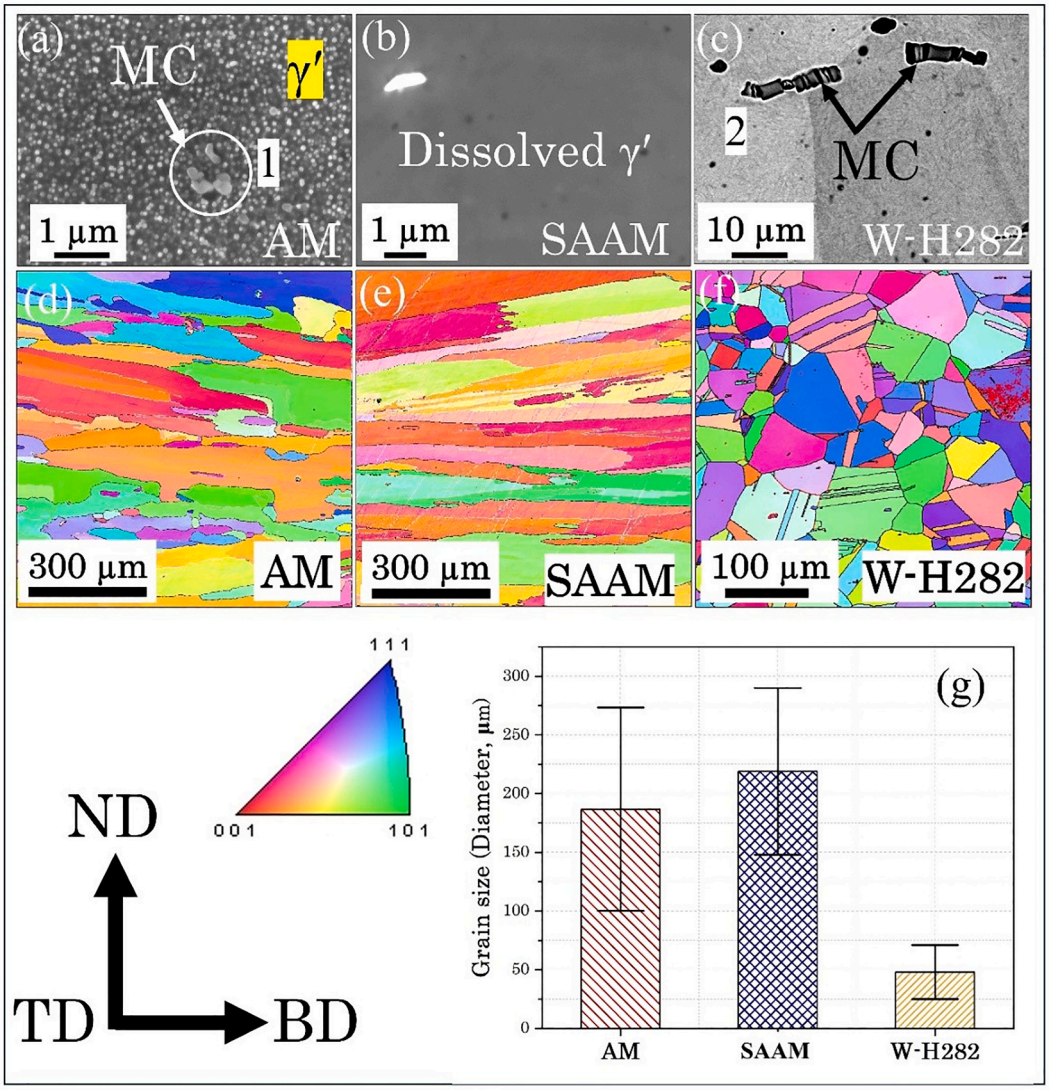

Fig. 2. SEM micrographs and EBSD IPF maps of (a,d) as-built AM, (b,e) SAAM, and (c,f) W-H282 starting materials, respectively, and (g) average grain size of starting materials.

Table 3
EDS elemental composition of analysis points shown in Figs. 2(a) and (c) (at.%).

Analysis point	Ti	Al	Cr	Mo	Ni
1- MC	19.62	1.33	17.48	17.22	Bal.
2- MC	54.98	–	3.09	36.98	Bal

free from γ′ precipitates in the as-welded condition.

Fig. 3(b-d) displays the surface profiles of the welds made with AM, SAAM, and W-H282 alloys. Interestingly, in the SAAM and W-H282 alloys, a significant thinning of the weld zone on the advancing side (AS) is observed due to the asymmetrical material flow associated with the hemispherical shoulder profile and tool tilt toward the retreating side (RS) [26]. The primary causes for the thinning on the advancing side are the high material fluidity (due to elevated temperatures) and the absence of a flat shoulder, which typically constrains material flow at the tool periphery [27,28]. Consequently, hot material exits the weld zone in the form of flash. Plastic deformation is more easily facilitated when the material just ahead of the tool has lower strength (or hardness). This leads to the larger flash observed in the SAAM and W-H282 alloys compared to the γ′ precipitation-hardened AM alloy. This is reflected in the relatively uniform weld profile and reduced flash thickness in the AM alloy. Fig. 3(e) presents the axial load profile during FSW. A consistent axial load of approximately 12 kN was observed throughout the linear tool travel, indicating stable welding conditions for all three states of the H282 alloy.

3.3. *Microstructural evolution*

(i) ***As-welded condition***

Fig. 4 (a-d) displays the SZ microstructure of the AM-FSW, SAAM-FSW, and W-H282 FSW specimens, respectively. Notably, the SEM micrographs represented in Fig. 4 were obtained at the same magnification as that of Fig. 2 (a-b) to compare the microstructural constituents of the as-welded specimen with the respective starting materials. The microstructure of the AM-FSW specimen (Fig. 4(a)) confirms the dissolution of the γ′ precipitates in the welded region of the specimen. Moreover, the fine primary MC carbides observed in Fig. 2(a)(AM specimen) were not observed in the AM-FSW specimen. The welding temperature of ~ 1050 °C is unlikely to dissolve these Ti and Mo-rich MC carbides. However, the shear stresses caused by high material flow during FSW may have fragmented these fine MC carbides into ultra-fine carbides [29]. Therefore, it becomes difficult to confirm the presence of these

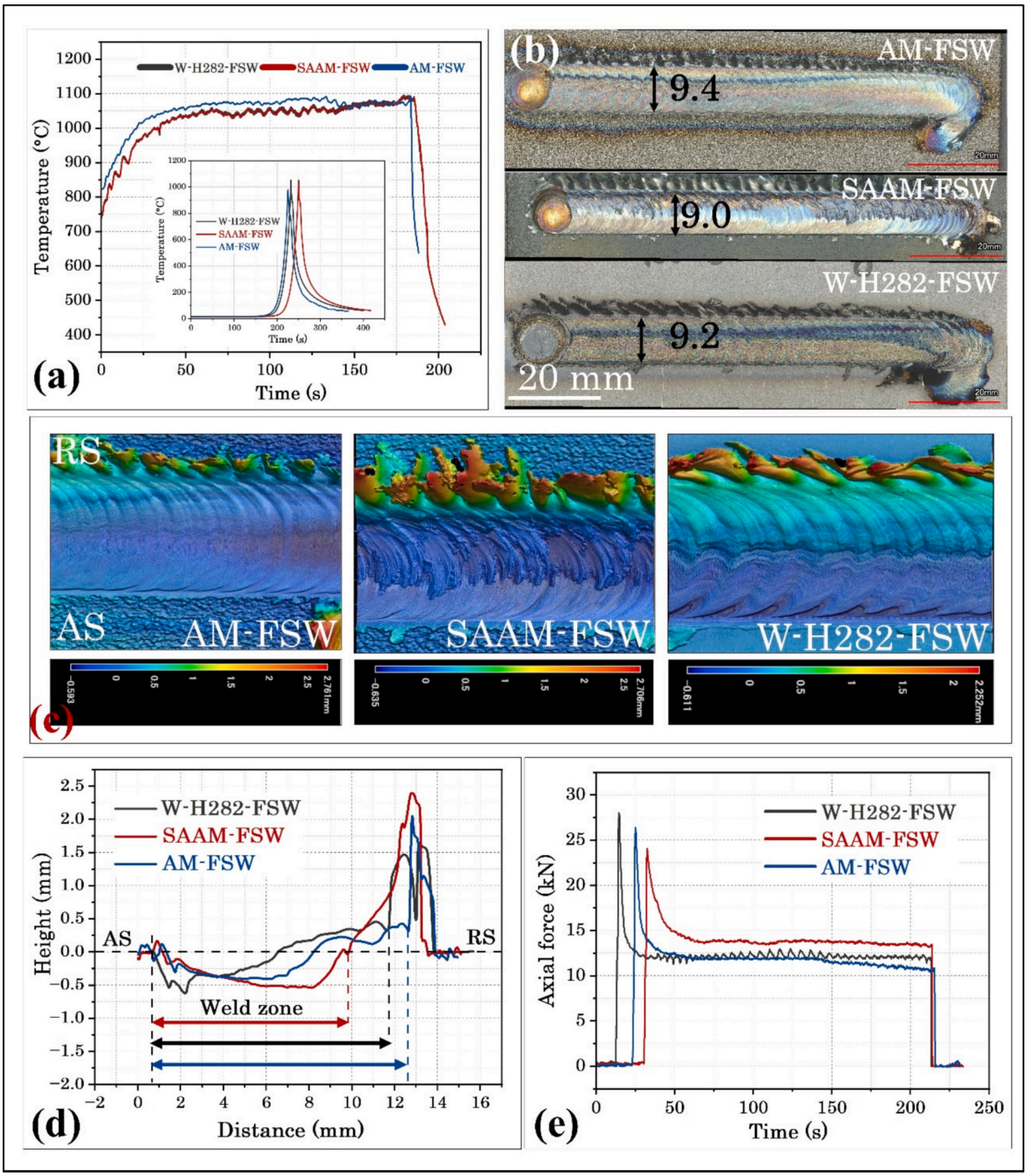

Fig. 3. (a) Temperature profile, (b-c) Qualitative weld surface profile, (d) quantitative weld profile, (e) axial force profile during FSW of as-welded AM, SAAM, and W-H282.

carbides in the SZ of the AM-FSW specimen. Comparing Figs. 2(c) and 4(d), the fracture and redistribution of MC carbides in the W-H282-FSW specimen under the influence of high material flow stresses can be confirmed. The coarse intergranular MC carbides dispersed in the form of interconnected colonies in the W-H282 specimen (Fig. 2(c)) are redistributed as fine and singly dispersed carbides in the W-H282-FSW specimen (Fig. 4(d)). The fine MC carbide phases were also confirmed in the SAAM-FSW specimen as shown in Fig. 4(b). The EDS analysis represented in Table 4 further confirms this carbide phase as Ti and Mo-rich MC carbides. To summarize, the as-welded specimens in all three states of H282 alloy consist of finely dispersed MC carbides and no traces of γ' precipitates in the welded zone.

(ii) ***Post-weld heat treatment***

Fig. 5 (a–b), (c–d), and (e–f) present the backscattered electron (BSE-SEM) micrographs of the PWHT AM-FSW, SAAM-FSW, and W-H282-FSW specimens, respectively. Table 5 and Fig. 4s (supplementary information) provide the corresponding point EDS analyses and elemental maps, respectively. These results confirm the presence of Mo-rich MC carbides and secondary Cr-rich $M_{23}C_6$ carbides as the key constitutional phases in all the PWHT specimens shown in Fig. 5. The $M_{23}C_6$ carbides were observed to nucleate preferentially along grain boundaries as discrete, fine particles. EDS analysis (Table 5) further verifies these carbides as Cr-rich secondary carbide phases.

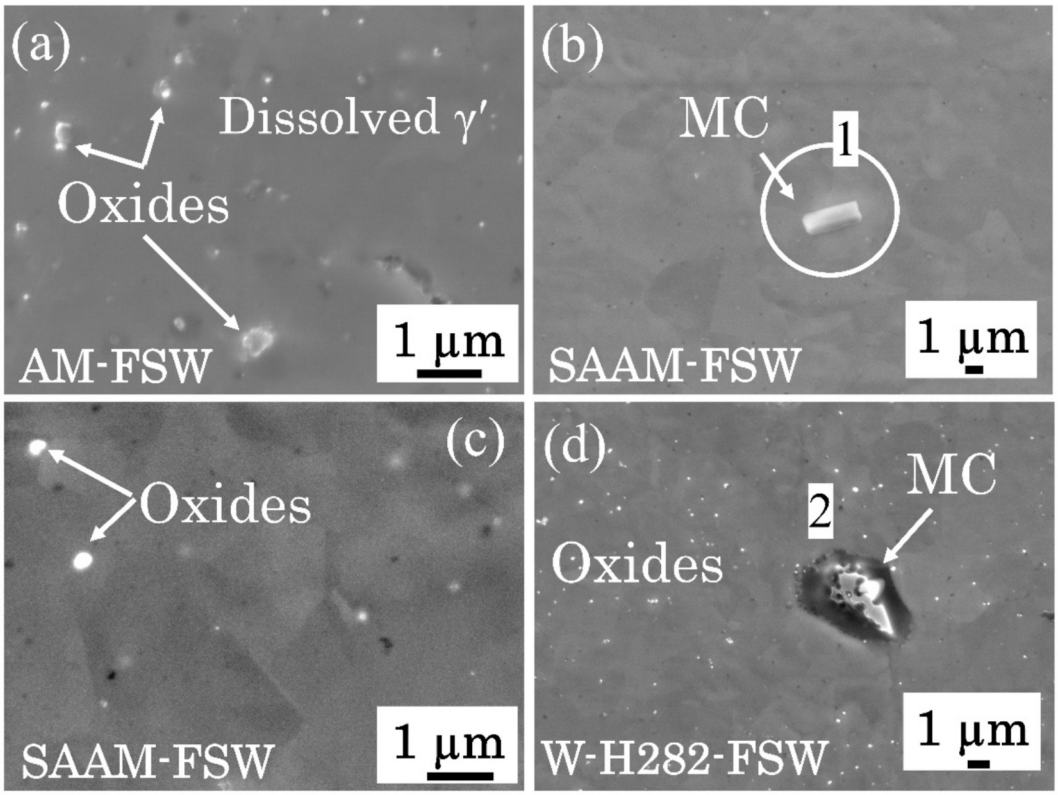

Fig. 4. SEM micrographs of the SZ of as-welded (a) AM-FSW, (b-c) SAAM-FSW (d) W-H282-FSW specimens.

Table 4
EDS point analysis corresponding to the sites shown in Fig. 4 (b) and (d) (at.%).

Analysis point	Ti	Al	Cr	Mo	Ni
SAAM-FSW					
1- MC	1.98	1.21	18.30	32.88	Bal
W-H282-FSW					
2- MC	63.69	–	2.61	28.40	Bal.

Interestingly, although the hardness mapping (Fig. 11, discussed later) indicates a significant increase in hardness following PWHT, fine γ′ precipitates were not visible in the SEM micrographs shown in Fig. 5. This absence is attributed to the extremely fine, nanometric scale of the γ′ precipitates, which falls below the resolution capability of standard SEM imaging. As a result, TEM analysis was carried out to confirm the presence of γ′ nano-precipitates in the weld zone of the PWHT specimens.

3.4. TEM analysis

The TEM analysis was conducted on the as-built AM specimen (starting material) and the SZ region of the AM-PWHT specimen. Fig. 6 shows the TEM micrographs and corresponding EDS maps of the as-built AM specimen. Figs. 6(a) and (d) show the bright field (BF) TEM micrographs of the specimen depicting a dense distribution of γ′ precipitates in the matrix. The particle size distribution in Fig. 9 (later in the paper) confirms the average size of the precipitates to be ~ 69 nm. The selected area diffraction (SAD) pattern in Fig. 6 (b) confirms the coherency between the γ′ precipitates and the austenitic γ matrix. The dark field TEM micrograph of the precipitates, along with the Fast Fourier transform (FFT), is also shown in Fig. 6(c). Fig. 6(e) shows the specimen's EDS elemental mapping, where fine Ti-rich MC carbides can be visualized. Additionally, the high contrast of Ti and Al in Fig. 6(e) further confirms the precipitates as Ti- and Al-rich γ′ precipitates.

Fig. 7 shows the BF-TEM micrographs of the SZ of the AM-PWHT specimen. Fig. 7(a) shows the distribution of MC carbides and finely dispersed γ′ precipitates in the SZ of the welded specimen. The precipitation of fine Cr-rich $M_{23}C_6$ carbides at the grain boundaries and other MC carbides is also shown in Fig. 7(d). Figs. 7(b) and (c) show the high magnification BF-TEM micrographs representing dense dispersion of extremely fine γ′ precipitates. However, the fine precipitates are beyond the resolution of the microscope for further analysis such as particle size measurement and diffraction pattern analysis. Therefore, High-Angle Annular Dark-Field micrographs (HAADF) are obtained from a high resolutiuon treansmission electron microscope as shown in Fig. 8. The dark contarst sphere shaped particles in Fig. 8 (a-c) are confirmed as a γ′ precipitates through a selected area electron diffraction (SAED) pattern (Fig. 8(f)). The presence of MC carbides can be visualized in Fig. 8(d) with a corresponding diffraction pattern shown in Fig. 8(e). The average size of the γ′ precipitates in the SZ as measured from the HAADF micrographs is around 24 nm (see Fig. 9 (b)). Fig. 10 (a1-a7) shows the EDS mapping confirming the identified carbide phases as Ti- and Mo-rich MC carbides and Cr-rich $M_{23}C_6$ carbides. Fig. 10 (b1-b3) shows the EDS elemental mapping from thr HAADF micrographs further confirming the fine precipitates as Ti- and Al-rich γ′ precipitates.

3.5. Grain refinement

Fig. 11 (a-c) and (d-f) represent the EBSD IPF maps of as-welded and PWHT specimens, respectively. Fig. 11 (g) shows the variation of average grain size in the SZ of various specimens in the as-welded and PWHT conditions. Firstly, an extensive grain refinement is observed in the welded specimens (both as-welded and PWHT) as compared to the starting materials (Fig. 2 (g)). As-built AM specimen's grain size is refined from ~ 170 μm in the starting material (AM) to ~ 7–8 μm in the SZ of AM-FSW and AM-PWHT specimens. Similarly, the grains are refined from ~ 220 μm in the SAAM specimen to ~ 5 μm in the SAAM-FSW and SAAM-PWHT specimens. The trend continues for the wrought

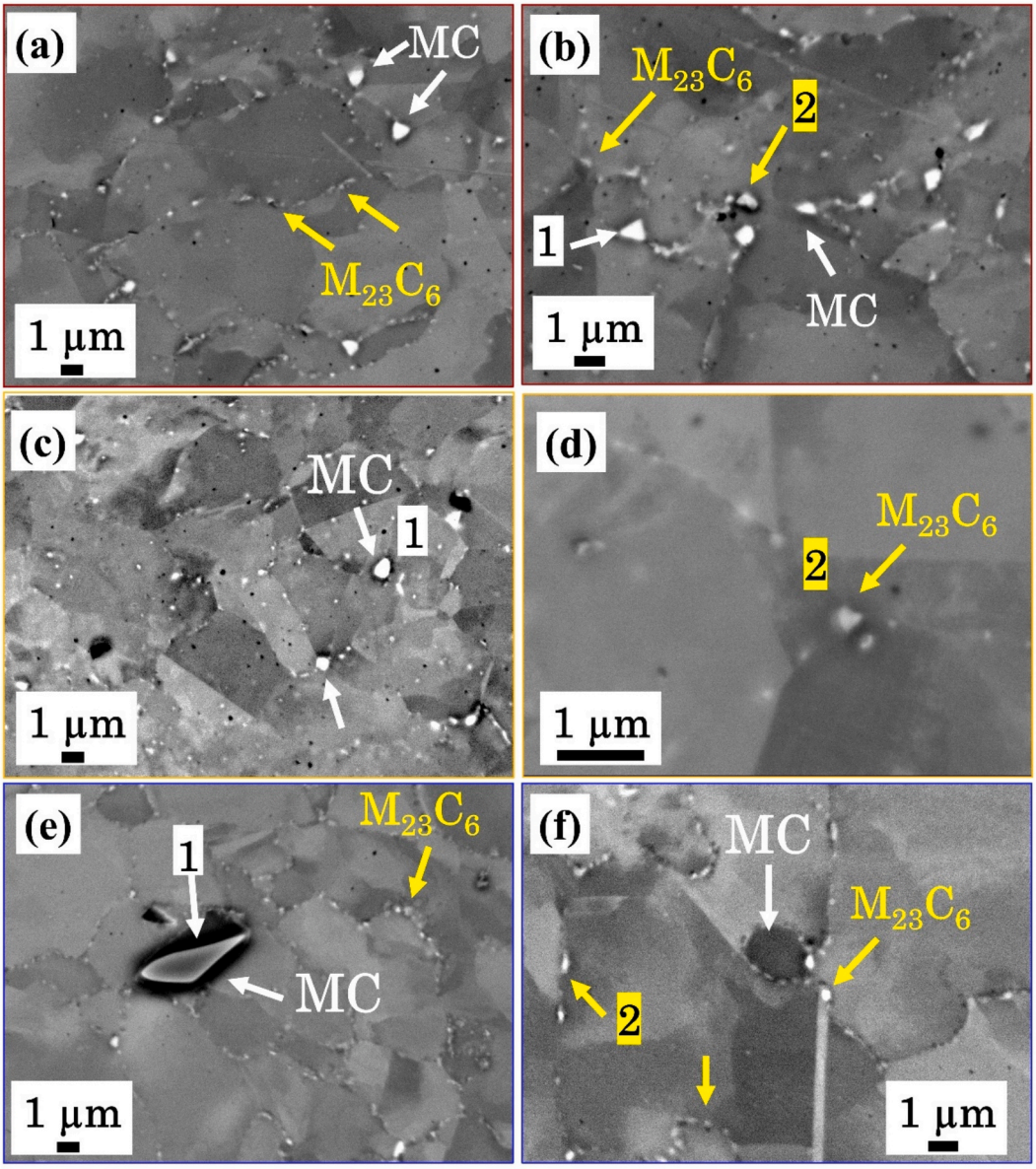

Fig. 5. BS-SEM micrographs of (a-b) AM- PWHT, (c-d) SAAM- PWHT, and (e-f) W-H282-PWHT specimens.

Table 5
EDS point analysis corresponding to the sites shown in Fig. 5 (at.%).

Analysis point	Al	Ti	Cr	Mo	Ni
AM-PWHT					
1-MC	0.71	2.62	22.21	37.62	Bal.
2-$M_{23}C_6$	1.28	6.15	28.27	8.20	Bal
SAAM-PWHT					
1-MC	0.82	2.42	21.92	32.86	Bal.
2-$M_{23}C_6$	1.34	2.46	38.97	12.40	Bal.
W-H282-PWHT					
1-MC	–	55.99	3.44	34.57	Bal.
2-$M_{23}C_6$	1.04	2.17	45.25	11.78	Bal

specimen, where the grains are refined from ~ 48 μm in the W-H282 specimen to ~ 6–8 μm in the W-H282-FSW and W-H282-PWHT specimens. The significant grain refinement in all the specimens is attributed to the dynamic recrystallization during FSW [30]. Interestingly, in the PWHT specimens, the grain size is almost similar to that of the as-welded condition, even after exposure to a high temperature for a prolonged duration. This phenomenon is attributed to the precipitation of Cr-rich $M_{23}C_6$ carbides at the grain boundaries during the first stage of PWHT specimens [31]. These fine-grain boundary secondary carbides stabilize the grain boundary for the second stage of PWHT specimen (and consequently creep resistance) and thus avoid any significant grain coarsening.

3.6. Mechanical properties

Fig. 12 (a, c, e) and (b, d, f) present the microhardness maps of the as-welded and PWHT specimens, respectively. The as-welded specimens (Fig. 12(a, c, e)) exhibit three distinct regions: SZ, HAZ, and the base metal zone (BMZ). Additionally, an intermediate zone (IZ) with relatively higher hardness than the HAZ, indicated by a turquoise-blue color, appears between the HAZ and BMZ in the as-welded condition.

The SZ shows higher hardness in the W-H282-FSW and SAAM-FSW specimens as compared to the respective base material. This increase is mainly due to grain refinement resulting from dynamic recrystallization during the FSW process, as confirmed by the EBSD analysis in Fig. 11. In contrast, Fig. 12(e) shows that the SZ of the AM-FSW specimen has lower hardness than the base material. Notably, the starting

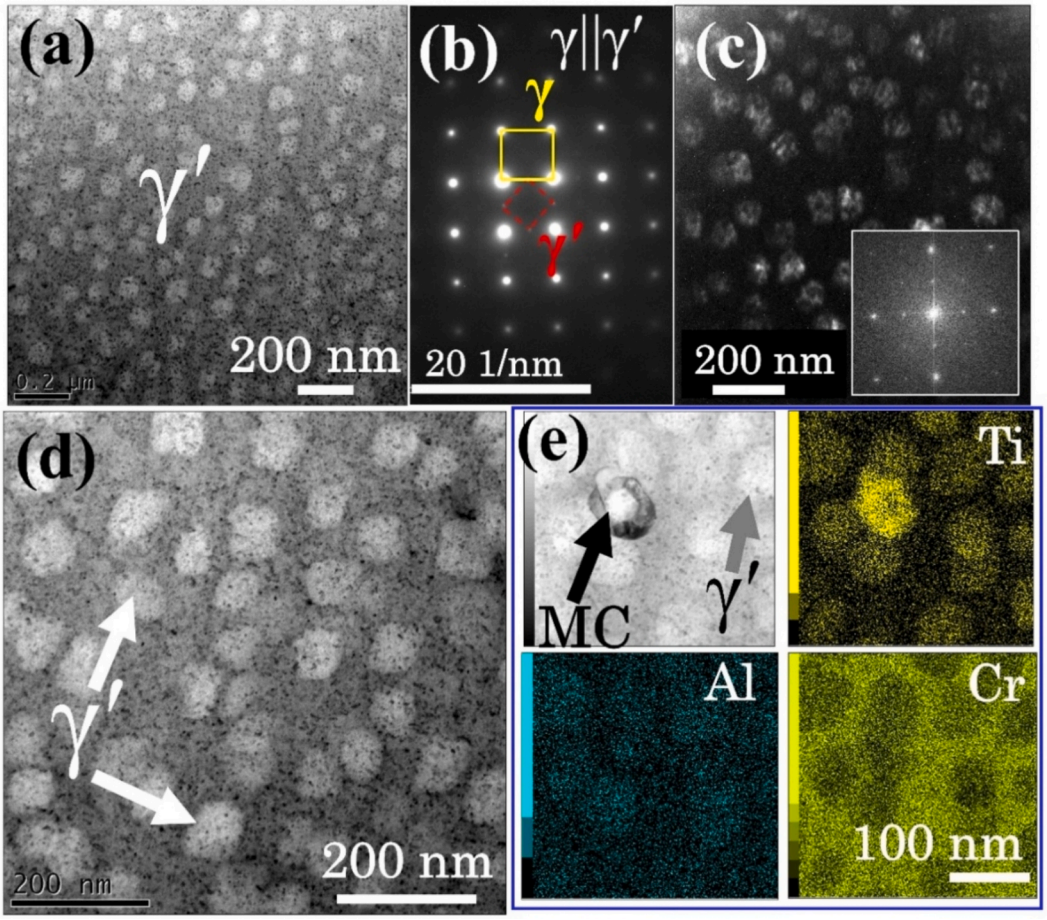

Fig. 6. (a,d) BF-STEM micrograph, (b) SAED pattern, (c) DF-TEM micrograph, and (e) EDS mapping of as-built AM specimen.

AM material is strengthened by γ′ precipitates, which were dissolved during FSW due to the heat input in the AM-FSW specimen, leading to a lower SZ hardness than the BMZ [32]. Nevertheless, despite the loss of γ′ precipitates in the SZ of the AM-FSW specimen, the resulting grain refinement contributes to a comparable hardness to that observed in the W-H282-FSW and SAAM-FSW specimens. Hence, the similar hardness levels in the SZ across all as-welded specimens suggest that grain refinement is the dominant mechanism enhancing hardness in the SZ [33,34].

The high hardness of the IZ between HAZ and BM of the as-welded W-H282-FSW and SAAM-FSW specimens is attributed to the precipitation of γ′ strengthening phase in this region. However, this IZ in the AM-FSW specimen demonstrates a lower hardness than the BMZ, which can be attributed to the growth of existing γ′ precipitate in this region.

To further confirm this hypothesis, the TEM specimen was obtained from this IZ of the AM-FSW specimen as shown in Fig. 13. Fig. 13 (a-d) shows the BF-TEM micrographs representing the distribution of γ′ and MC carbides in this intermediate region. Notably, in the AM-FSW specimen, this region already has a γ′ precipitate before the welding. However, the heat input during welding leads to a growth of precipitate size from 69 nm in the AM specimen to ~ 76 nm in this intermediate region, as shown in Fig. 13 (e). The growth in particle size reflects that the heat accumulated in this region is sufficient for the precipitation of γ′ in the W-H282-FSW and SAAM-FSW specimens, and the growth of the existing γ′ precipitates in the AM-FSW specimens.

The microhardness distribution of PWHT specimens (Fig. 12 (b.d.f)) shows an extremely high hardness of the SZ, HAZ, IZ, and BMZ regions of W-H282-PWHT and SAAM-PWHT specimens. However, in the AM-PWHT specimen, the PWHT leads to the precipitation of γ′ in the SZ and HAZ, along with the overaging of the BMZ, leading to a reduced hardness as compared to the starting material. The extremely high hardness of the SZ in all the PWHT specimens is attributed to the combination of extremely fine grain size and γ′ precipitates.

Fig. 14 (a) and (b) present the nominal tensile stress–strain (SS) curves and the variation in average ultimate tensile strength (UTS) for the different specimens examined in this study. Table 6 summarizes the quantitative data from the SS curves in Fig. 14 (a). In all three states of the H282 alloy, the maximum tensile strength is observed in the PWHT specimens, followed by the FSWed specimens, and lastly, the starting material. The AM exhibits the highest UTS among the three starting materials, approximately 1000 MPa. This elevated strength is primarily attributed to the in-situ γ′ precipitation during EB-PBF. Conversely, the SAAM displays the lowest strength due to the dissolution of γ′ precipitates during the solution annealing process. The W-H282 specimen shows an intermediate strength, benefiting from work hardening and a fine-grained structure.

During FSW of the AM specimen, two competing phenomena occur within the SZ. First, the high temperatures generated during welding lead to the dissolution of γ′ precipitates. At the same time, dynamic recrystallization occurs, resulting in the formation of a fine-grained structure and a dislocation pileup. Consequently, while the dissolution of γ′ precipitates reduces strength, the formation of fine grains and dislocation structures enhances it. This balance leads to a favorable combination of strength and ductility in the SZ of AM-FSW specimen. In contrast, in the SZs of SAAM-FSW and W-H282-FSW specimens, only strengthenings by grain refinement and dislocations dominate. This observation is further supported by calculations of the individual contributions from various strengthening mechanisms, as discussed in the next section.

Fig. 15 presents the low magnification fractographs of the tensile

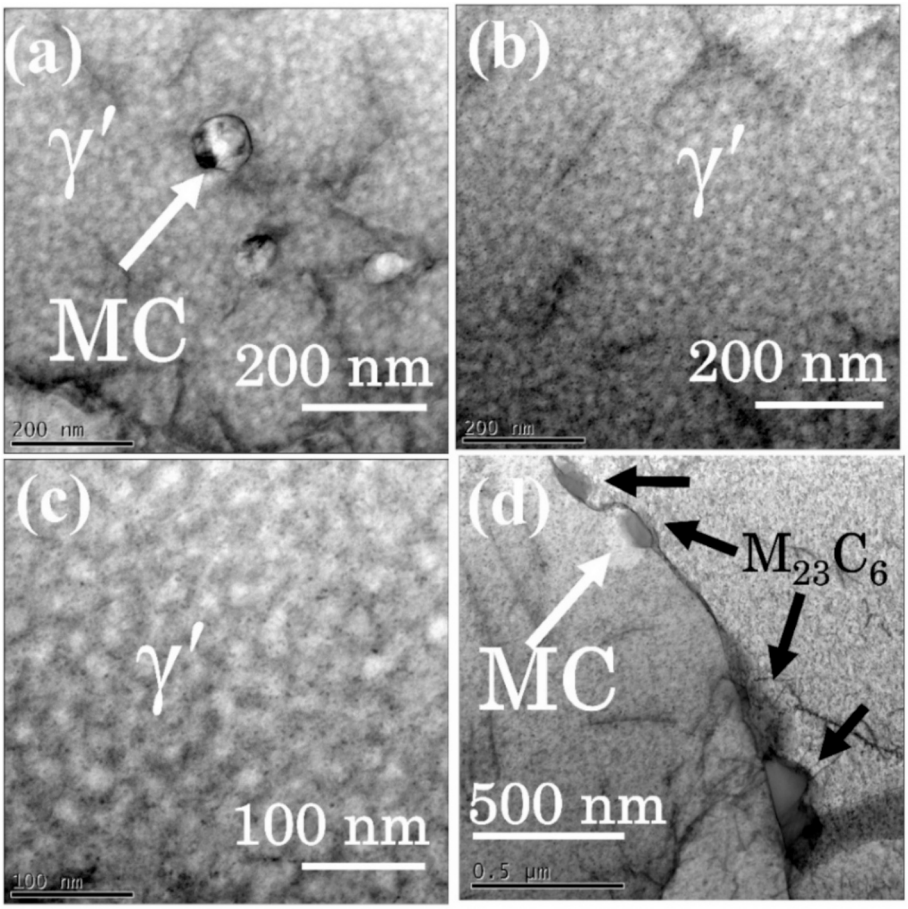

Fig. 7. BF-STEM micrographs of the SZ of the AM-PWHT specimen.

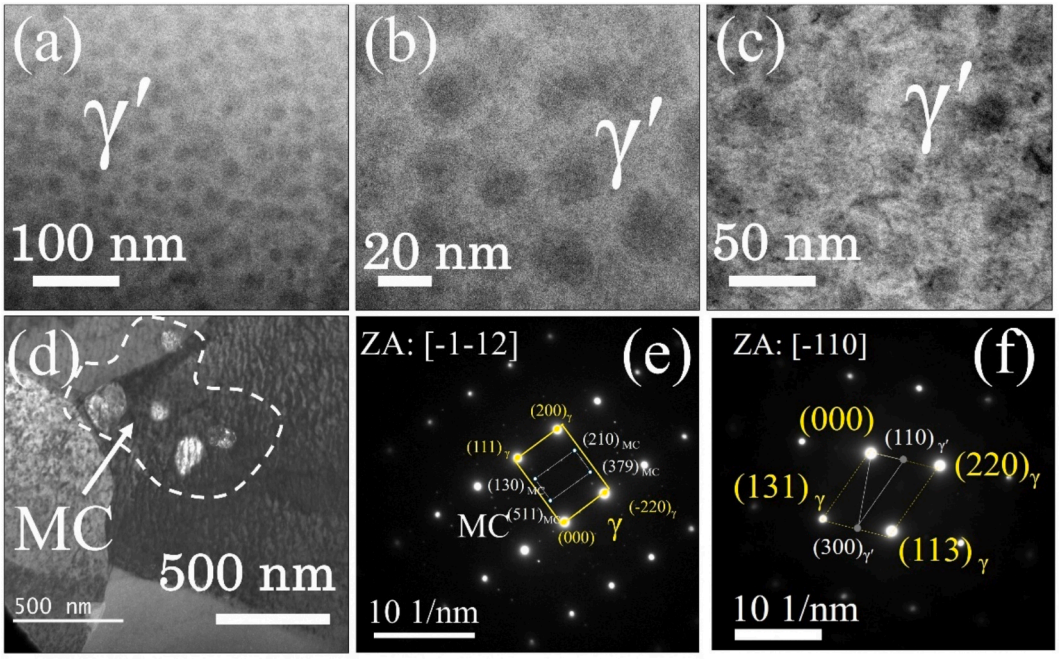

Fig. 8. (a-d) HAADF TEM micrographs, and (e-f) SAED micrographs from the SZ of AM-PWHT specimen.

specimens investigated in this study. The fractograph of the AM specimen (Fig. 15(a)) reveals a combination of fine dimples within the grain interior, large dimples, and cleavage facets. The large dimples are primarily attributed to gas pores and shrinkage porosity associated with the EB-PBF process. Fig. 1s (supplementary information) confirms the presence of significant porosity in the as-built AM structure,

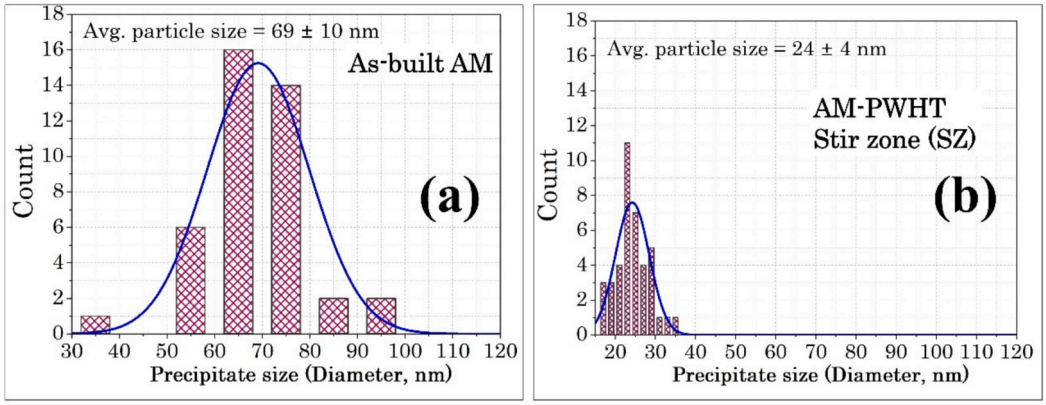

Fig. 9. Size distribution of γ′ precipitate in (a) as-built AM, and (b) AM-PWHT specimen.

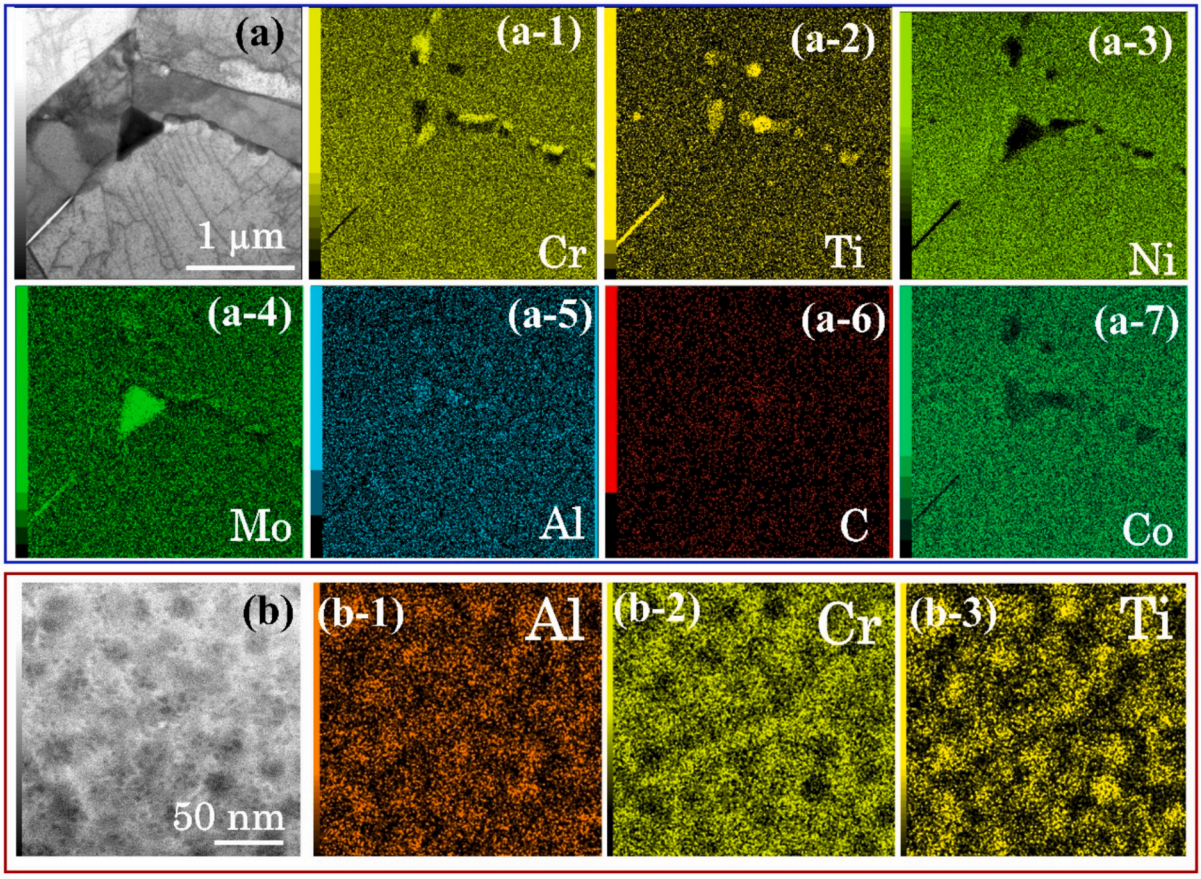

Fig. 10. TEM-EDS elemental mapping of (a) carbide phases (count map), and (b) γ′ precipitates (quantitative map) in the SZ of the AM-PWHT specimen.

contributing to elemental segregation. These pores act as localized stress concentration sites during uniaxial tensile loading, leading to a catastrophic fracture and low total elongation. These shrinkage porosities are eliminated in the SZ of the AM-FSW specimen due to adequate material mixing. The removal of porosity, combined with the extremely fine grain structure, results in very fine dimples in the fractured specimen, as seen in Fig. 15(d). The refined grains promote void nucleation at multiple sites, but restrict void growth, thereby enhancing the total elongation of the AM-FSW specimen compared to the AM specimen. Fig. 15(g) displays the fractograph of the AM-PWHT specimen, which shows dimples similar to those in the AM-FSW specimen. Notably, the AM-PWHT specimen contains fine Cr-rich $M_{23}C_6$ carbides at the grain boundaries and γ′ precipitates in the grain interior. During uniaxial tensile testing, the matrix/carbide interfaces act as preferential stress concentration sites, leading to void nucleation, propagation, and eventual growth, resulting in intergranular fracture.

Fig. 15(b) shows the fractograph of the starting material, the SAAM specimen. Similar to the AM specimen (Fig. 15(a)), shrinkage porosity-induced catastrophic fracture is observed. However, despite the similar porosity, the SAAM specimen exhibits greater elongation than the AM specimen. This phenomenon is attributed to the dissolution of γ′ precipitates and a corresponding reduction in hardness. As a result, increased dislocation accumulation occurs within the grains during tensile loading, promoting higher deformation (as evidenced by local

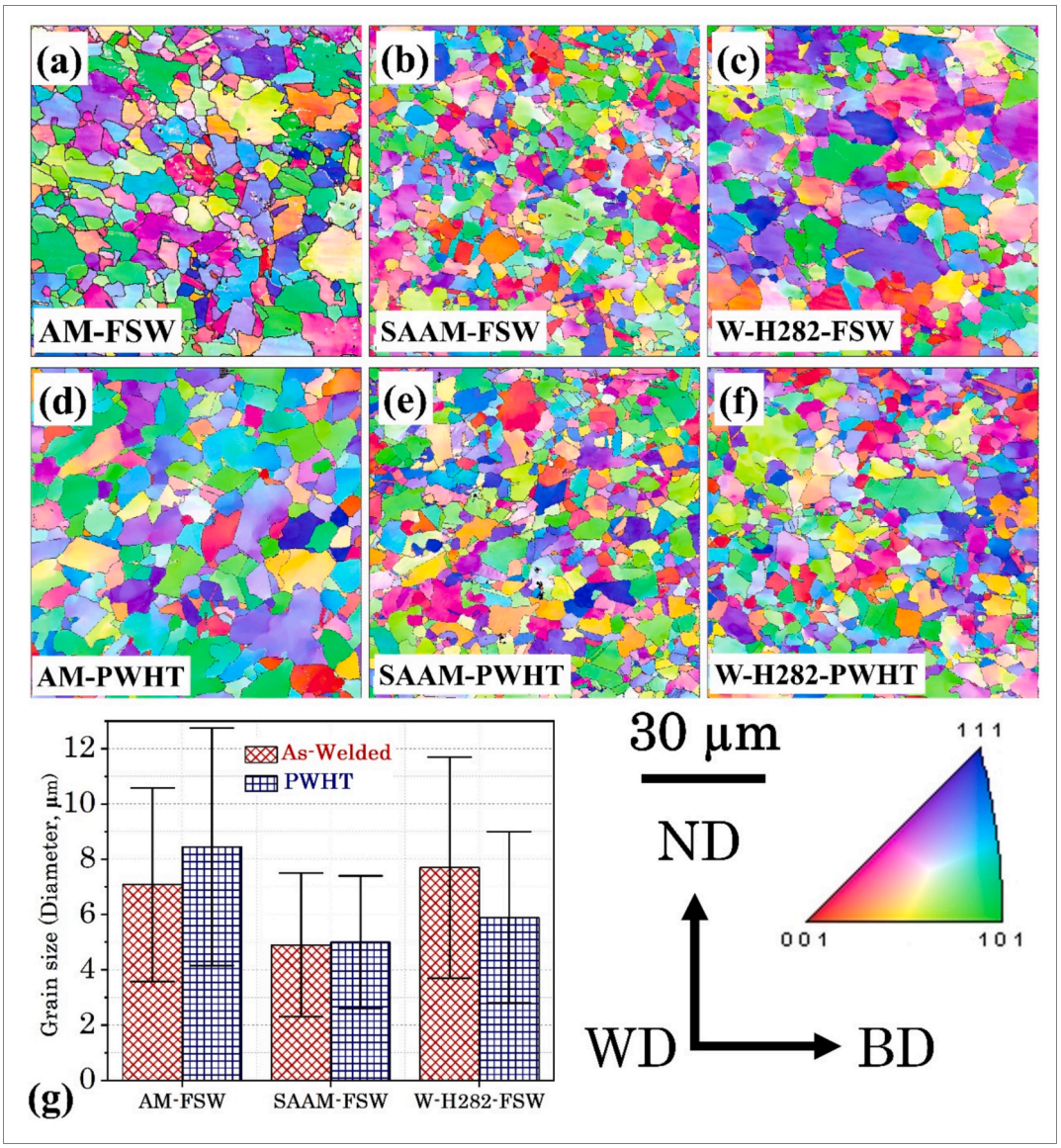

Fig. 11. EBSD-IPF maps of (a-c) as-welded, (d-f) PWHT specimens, and (g) average grain size distribution of various specimens.

elongation) and overall elongation. In the SAAM-FSW specimen, the key features include the absence of porosity and precipitates, along with a very fine-grained microstructure. Grain refinement increases hardness via the Hall–Petch mechanism, decreasing total elongation. The fractograph of the SAAM-PWHT specimen is comparable to that of the AM-PWHT specimen, owing to similar strengthening mechanisms in both.

Fig. 15(c) illustrates a coarse intergranular fracture in the W-H282 specimen, originating from intergranular coarse MC carbide colonies, as shown earlier in Fig. 2(c). FSW-induced material mixing transforms this interconnected carbide network into a distribution of uniformly dispersed carbides within the SZ, resulting in a mixed mode of intergranular and transgranular fracture as shown in Fig. 15(f). Lastly, the W-H282-PWHT specimen exhibits characteristics similar to the AM-FSW and SAAM-FSW specimens, leading to a comparable fractographic appearance, as shown in Fig. 15(i).

4. Discussion

4.1. Dominating strengthening mechanisms

The experimental yield strength shown in Table 6 can be compared with the theoretical strengthening contributions from multiple mechanisms involved in different specimens. The major strengthening mechanisms in this particular study are as follows: intrinsic or frictional strength of pure Ni (σ_0), grain boundary strengthening (σ_{gb}), solid solution strengthening (σ_{ss}), dislocation strengthening (σ_{ds}), and precipitation strengthening (σ_{ps}). Therefore, the theoretical yield strength (σ_b) can be expressed as:

$$\sigma_b = \sigma_0 + \sigma_{ss} + \sigma_{gb} + \sigma_{ds} + \sigma_{ps} \quad (1)$$

(i) *Intrinsic strength*

The intrinsic or frictional strength of the pure Ni can be evaluated by an empirical relation reported in the previous studies as follows [35]:

$$\sigma_0 = M\tau_{CRSS} \quad (2)$$

where M is denoted as the Taylor factor ($M = 3$ for FCC structure), and τ_{CRSS} is the critical resolved shear stress (17.5 MPa for Ni-based superalloys) [36]. Therefore, from eq. (2) the σ_0 can be evaluated to be ~ 52.5 MPa.

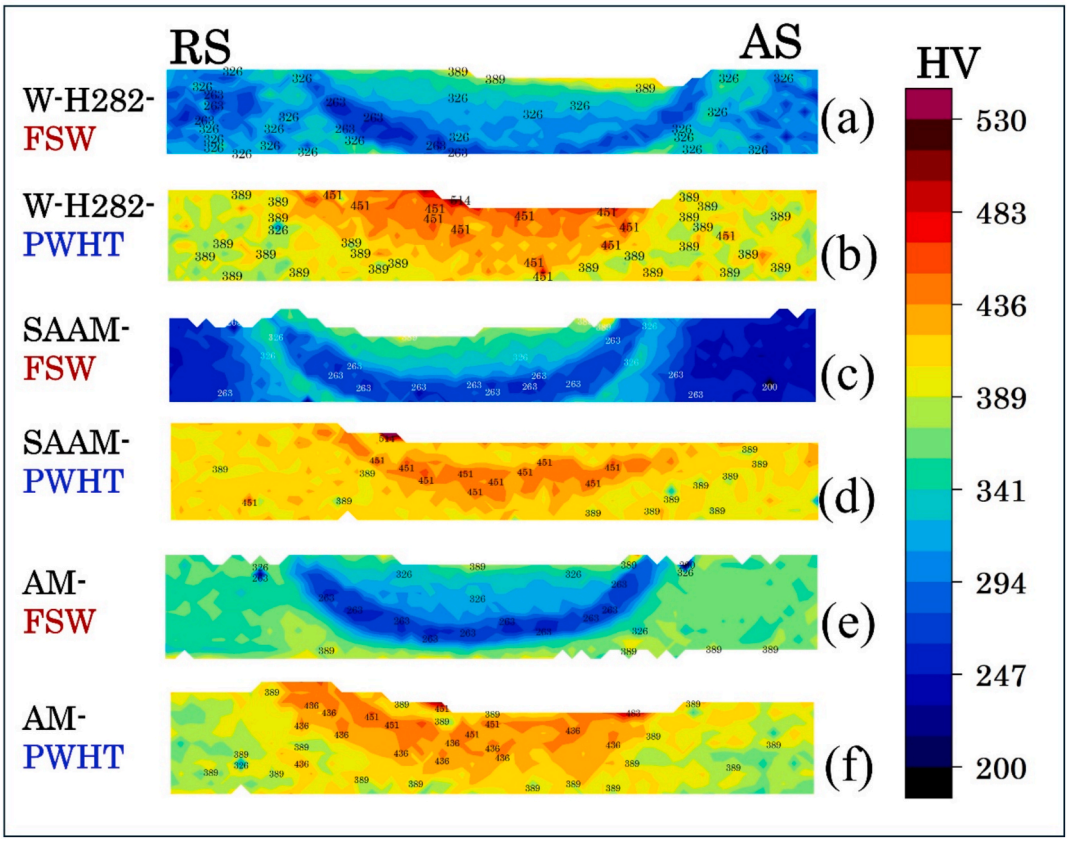

Fig. 12. Vickers microhardness mapping of as-welded and PWHT specimens.

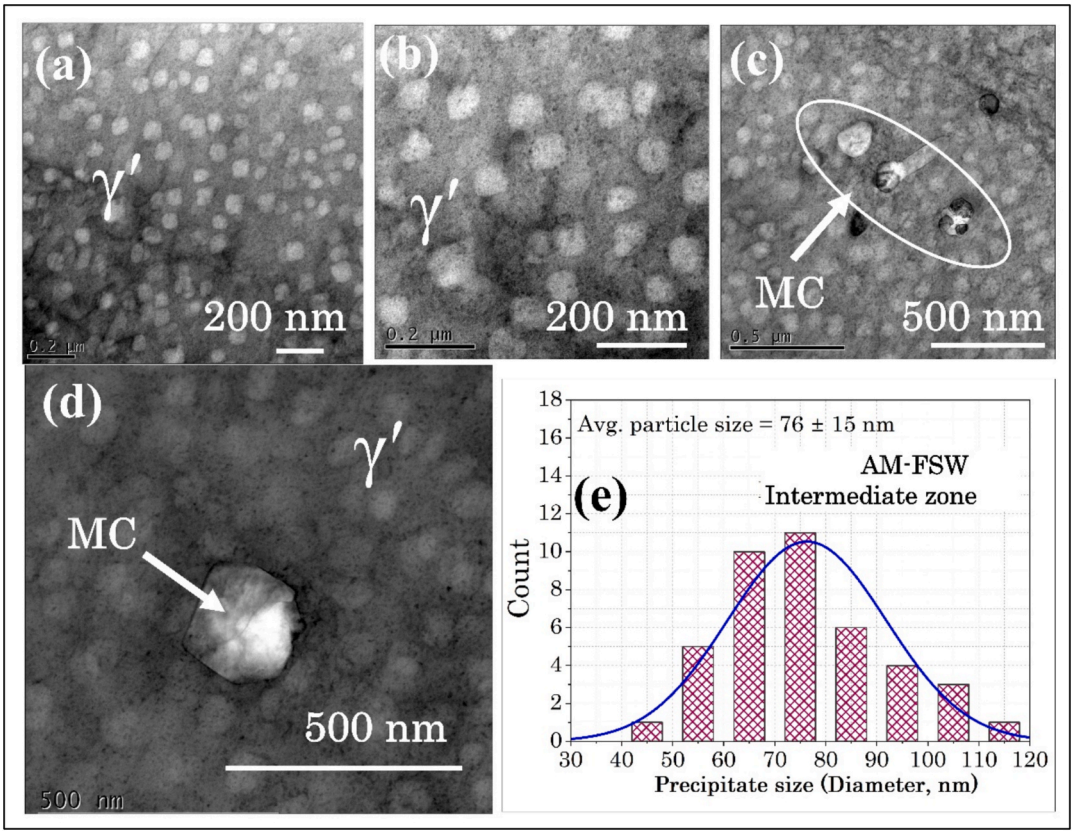

Fig. 13. (a-d) BF-STEM micrographs of the intermediate zone of the AM-FSW specimen, (e) size distribution of γ′ precipitates in the IZ.

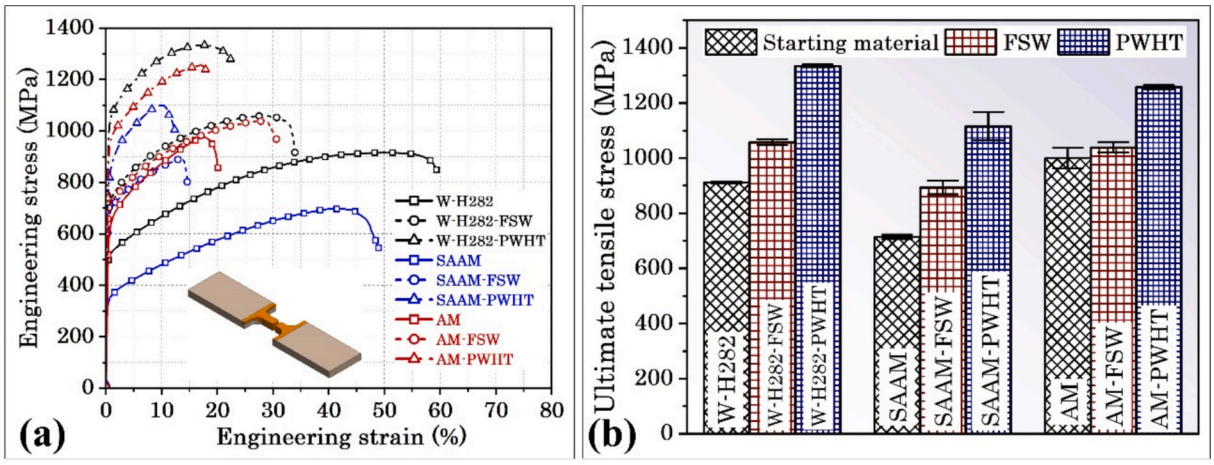

Fig. 14. (a) Tensile stress–strain plot, (b) average UTS of starting material, as-welded and PWHT specimens.

Table 6
Quantitative mechanical properties obtained from the nominal stress–strain curve.

Specimen	UTS (MPa)	YS (MPa)	TE (%)
W-H282	912 ± 4	503 ± 3	59.5 ± 0.3
W-H282-FSW	1058 ± 11	702 ± 6	34.8 ± 2.1
W-H282-PWHT	1335 ± 5	1027 ± 3	23.0 ± 0.1
SAAM	714 ± 8	330 ± 2	50.3 ± 8.5
SAAM-FSW	894 ± 25	659 ± 13	15.7 ± 3.0
SAAM-PWHT	1116 ± 52	826 ± 44	12.9 ± 0.1
AM	1000 ± 38	608 ± 14	24.7 ± 5.6
AM-FSW	1039 ± 18	692 ± 15	33.4 ± 4.5
AM-PWHT	1258 ± 7	937 ± 5	26.0 ± 1.8

(ii) *Solid-solution strengthening*

The solid solution strengthening by different elemental constituents can be expressed as follows [37]:

$$\sigma_{ss} = \left[\sum \left(a_i c_i^{1/2}\right)^2\right]^{1/2} \tag{3}$$

where a_i is the strengthening constant for the solute atom i and c_i is the concentration of solute atom i. However, since H282 is a precipitation-strengthened alloy and the contribution of solid solution strengthening is marginal, it can be neglected in the present study [38].

(iii) *Grain boundary strengthening*

The grain refinement owing to the severe plastic deformation induced during FSW resulted in significant strengthening contributions through Hall-Petch relations in the FSWed and PWHT specimens of all three states of H282 alloy. The strengthening contribution through this grain boundary strengthening mechanism can be mathematically calculated as follows [39]:

$$\sigma_{gb} = \frac{k}{\sqrt{d_0}} \tag{4}$$

where k is the Hall-Petch coefficient equal to 750 MPa $\mu m^{1/2}$ in Ni-based superalloys, and d_0 is the average grain size (Fig. 11(g)) [40].

(iv) *Precipitation strengthening*

The interaction of precipitates and dislocations can be governed by two possible mechanisms based on the particle size, i.e., Orowan looping and precipitate cutting [41]. The Orowan looping dominates later when the precipitate size is greater than 140 nm, whereas the particle shearing dominates in the case of fine precipitates [36]. In the present investigation, the γ' particle size is well below 140 nm (as confirmed from Fig. 9), which indicates the dominance of the particle shearing mechanism. The shearing mechanism is primarily governed by the precipitate/matrix coherency and the order strengthening [42]. In the H282 alloy, the coherent strengthening resulting from the fine γ' can be considered as an overall precipitation strengthening, ignoring the strengthening contribution from the incoherent precipitates. Mathematically, the coherent precipitation strengthening can be represented as follows [35]:

$$\sigma_{ps} = 3MG\delta\left[\frac{Rf}{b}\right]^{1/2} \tag{5}$$

where G is the shear modulus, δ is the lattice mismatch between the precipitate and matrix, R is the size of γ' precipitates, f is the volume fraction of precipitates, and b is the magnitude of the Burgers vector.

The volume fraction and size of the precipitates were determined from the TEM micrographs. TEM analysis was performed only for the as-built AM specimen and the AM-FSW-PWHT specimen. However, since the W-H282-PWHT and SAAM-PWHT specimens underwent the same PWHT as the AM-PWHT specimen, it can be assumed that their σ_{ps} values are comparable to those of the AM-PWHT specimen.

(v) *Dislocation strengthening*

Dislocation strengthening can be mathematically represented by using a Taylor hardening relationship as a function of dislocation density as follows [43]:

$$\sigma_{ds} = \alpha MbG\rho^{1/2} \tag{6}$$

where α is a coefficient based on the cubic structure of the alloy, b represents the magnitude of the Burgers vector, G is the shear modulus of the H282 alloy, and ρ is the dislocation density.

Furthermore, the density of geometrically necessary dislocations (ρ) can be calculated from the Kernel Average Misrorientation (KAM) as follows [44]:

$$\rho = \frac{2KAM_{ave}}{ub} \tag{7}$$

where KAM_{ave} is the average misorientation angle in radians (calculated to the 1st neighbour), and u is the unit length (step size).

Based on these estimations, the comparison between the various theoretical strengthening contributions and the experimental strengths is presented in Fig. 16(a). For most specimens, the predicted

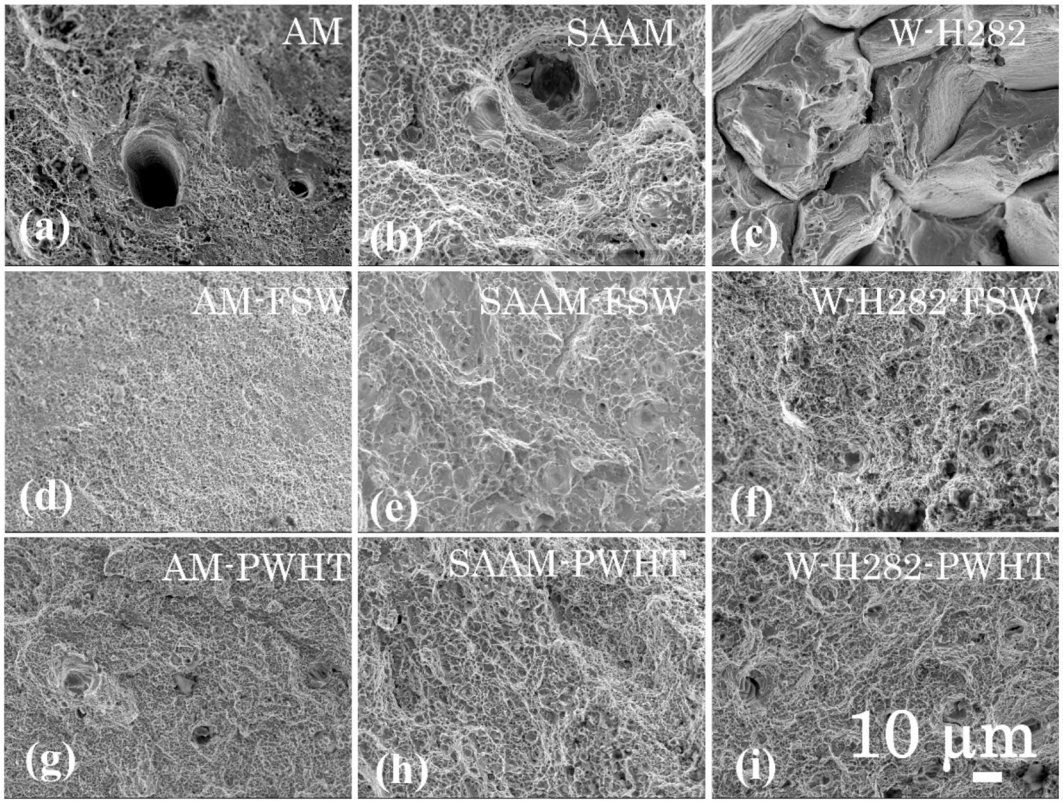

Fig. 15. SEM fractography of (a) as-built AM, (b) SAAM, (c) W-H282, (d) AM-FSW, (e) SAAM-FSW, (f) W-H282-FSW, (g) AM-PWHT, (h) SAAM-PWHT, and (i) W-H282-PWHT specimens.

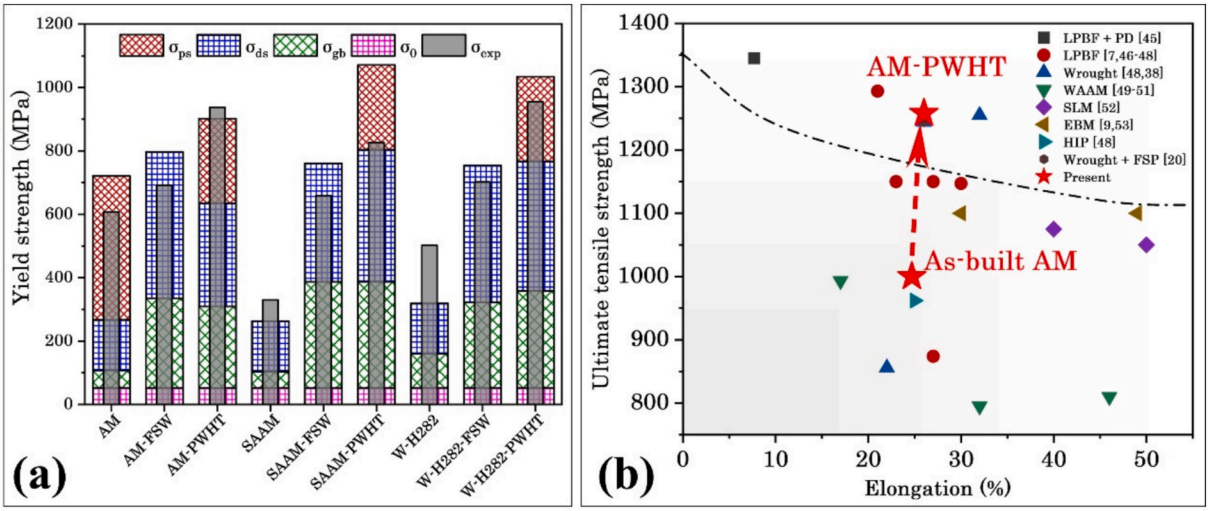

Fig. 16. (a) Theoretical contribution in strengthening from various mechanisms, and (b) comparison of present results with the previously available studies [7,38,45–53].

strengthening from different mechanisms aligns closely with the experimental yield strength, except in the cases of the SAAM-PWHT and W-H282 specimens. The significant deviations observed for these two specimens are likely due to uncertainties in the underlying assumptions, such as the inclusion of only geometrically necessary dislocations (GNDs) in the overall dislocation density calculations. Nevertheless, the dominant strengthening mechanisms in the as-welded specimens are the grain boundary strengthening and dislocation strengthening. Whereas, in the PWHT specimens, the grain boundary strengthening, dislocation strengthening, and precipitation strengthening all contribute significantly towards the overall strengthening of the joints. Fig. 16(b) represents the comparison of strength and elongation achieved in the present study with the previous studies involving additively manufactured H282 alloy (in precipitation hardened condition) with various fusion-based techniques. The application of FSW followed by PWHT significantly enhances the mechanical performance of the as-built AM specimen, shifting it toward a superior strength-ductility combination as shown in Fig. 16(b). This improvement highlights the advantage of FSW over conventional fusion-based methods. Consequently, FSW and related techniques such as friction stir processing (FSP) show strong

potential for crack repair and localized strengthening in additively manufactured H282 alloys.

5. Conclusions

In the present investigation, friction stir welding (FSW) using a novel hemispherical tool was conducted on three different types of Haynes 282 (H282) Ni superalloy: EB-PBF additively manufactured (AM) in the precipitation-hardened state, solution-annealed AM (SAAM), and soft-annealed wrought (W-H282) alloy. A UTS-based welding efficiency of 100 % was achieved for all three H282 alloy types. The key findings are summarized below:

- The heat generated during FSW was sufficient to dissolve the in-situ precipitated γ' in the SZ, resulting in a no-precipitate state in all three as-welded specimens.
- The severe plastic deformation during FSW led to dynamic recrystallization of grains in the SZ. The initial grain sizes of AM, SAAM, and W-H282 (~170 μm, 220 μm, and 54 μm, respectively) were refined to ~ 5–8 μm in the as-welded state. Furthermore, no significant grain growth was observed in the welded specimens after post-weld heat treatment (PWHT).
- In the as-welded state, Ti- and Mo-rich MC carbides were the only constituent phases observed. The TEM analysis confirmed the presence of γ' precipitates, Cr-rich $M_{23}C_6$ carbides at grain boundaries, and MC carbides in the SZ of the joints after PWHT. The γ' precipitates in the SZ after PWHT were extremely fine of ~ 24 nm in size, compared to ~ 69 nm for the in-situ EB-PBF γ' precipitates in the starting AM alloy.
- The hardness mapping demonstrated the presence of a wide heat-affected zone (HAZ) with low hardness values in the as-welded specimens. Following the PWHT, these softened zones were recovered with increased hardness values owing to the precipitation of γ' phase.
- The strength of the as-welded specimens for AM, SAAM, and W-H282 was 16 %, 25 %, and 4 % higher than that of their respective starting materials. After PWHT, the tensile strengths of AM, SAAM, and W-H282 specimens increased by ~ 46 %, 56 %, and 25 %, respectively, over their starting conditions.
- The enhanced strength in the as-welded specimens is attributed to grain boundary strengthening and dislocation strengthening. In contrast, the high strength of the PWHT specimens is due to a combination of grain boundary strengthening, dislocation strengthening, and precipitation strengthening.

CRediT authorship contribution statement

Abhishek Sharma: Writing – original draft, Resources, Project administration, Methodology, Investigation, Funding acquisition, Formal analysis, Conceptualization. **Sukhdeep Singh:** Writing – review & editing, Visualization, Validation, Resources. **Yoshiaki Morisada:** Resources, Supervision, Validation, Visualization, Writing – review & editing. **Kohsaku Ushioda:** Resources, Supervision, Validation, Visualization, Writing – review & editing. **Joel Andersson:** Funding acquisition, Resources, Writing – review & editing. **Hidetoshi Fujii:** Funding acquisition, Project administration, Resources, Supervision, Validation, Visualization, Writing – review & editing.

Declaration of competing interest

The authors declare that they have no known competing financial interests or personal relationships that could have appeared to influence the work reported in this paper.

Acknowledgment

AS: Acknowledge the financial support by a Grant-in-Aid for Scientific Research (KAKENHI) from the Japan Society for Promotion of Science (Grant Number 24 K17532) and a 2024 Research & Development Grant from the Kyoto Technoscience Center (Grant Number J245403003). SS and JA would like to acknowledge the funding support received from Västra Götalandsregionen, Tillväxtverket, European Regional Development Fund, and GKN Aerospace Sweden through the Spacelab project (grant number 20201639). The authors thank Mr. Jonas Olsson at University West for producing the specimens and the members of the Research Center for Ultra-High Voltage Electron Microscopy (UHVEM), The University of Osaka, for the assistance with the TEM analysis.

Appendix A. Supplementary data

Supplementary data to this article can be found online at https://doi.org/10.1016/j.matdes.2025.115029.

Data availability

Data will be made available on request.

References

[1] K.L. Kruger, HAYNES 282 alloy, in: Materials for Ultra-Supercritical and Advanced Ultra-Supercritical Power Plants, Elsevier, 2017: pp. 511–545. https://doi.org/10.1016/B978-0-08-100552-1.00015-4.
[2] B. Lim, H. Chen, K. Nomoto, Z. Chen, A.I. Saville, S. Vogel, A.J. Clarke, A. Paradowska, M. Reid, S. Primig, X. Liao, S.S. Babu, A.J. Breen, S.P. Ringer, Additively manufactured Haynes-282 monoliths containing thin wall struts of varying thicknesses, Addit. Manuf. 59 (2022) 103120, https://doi.org/10.1016/j.addma.2022.103120.
[3] H. Matysiak, M. Zagorska, J. Andersson, A. Balkowiec, R. Cygan, M. Rasinski, M. Pisarek, M. Andrzejczuk, K. Kubiak, K. Kurzydlowski, Microstructure of Haynes® 282® superalloy after vacuum induction melting and investment casting of thin-walled components, Materials 6 (2013) 5016–5037, https://doi.org/10.3390/ma6115016.
[4] R. Otto, V. Brøtan, P.A. Carvalho, M. Reiersen, J.S. Graff, M.F. Sunding, O.Å. Berg, S. Diplas, A.S. Azar, Roadmap for additive manufacturing of HAYNES® 282® superalloy by laser beam powder bed fusion (PBF-LB) technology, Mater. Des. 204 (2021) 109656, https://doi.org/10.1016/j.matdes.2021.109656.
[5] A. Ramakrishnan, G.P. Dinda, Microstructure and mechanical properties of direct laser metal deposited Haynes 282 superalloy, Mater. Sci. Eng. A 748 (2019) 347–356, https://doi.org/10.1016/j.msea.2019.01.101.
[6] H. Zhang, Y. Wang, R.R. De Vecchis, W. Xiong, Evolution of carbide precipitates in Haynes® 282 superalloy processed by wire arc additive manufacturing, J. Mater. Process. Technol. 305 (2022) 117597, https://doi.org/10.1016/j.jmatprotec.2022.117597.
[7] A.S. Shaikh, F. Schulz, K. Minet-Lallemand, E. Hryha, Microstructure and mechanical properties of Haynes 282 superalloy produced by laser powder bed fusion, Mater. Today Commun. 26 (2021), https://doi.org/10.1016/j.mtcomm.2021.102038.
[8] S. Singh, J. Andersson, K. Kadoi, Microstructure gradient formation in electron-beam melting powder-bed fusion of a gamma-prime Ni-based superalloy, Mater. Charact. 205 (2023) 113370, https://doi.org/10.1016/j.matchar.2023.113370.
[9] K.A. Unocic, M.M. Kirka, E. Cakmak, D. Greeley, A.O. Okello, S. Dryepondt, Evaluation of additive electron beam melting of haynes 282 alloy, Mater. Sci. Eng. A 772 (2020) 138607, https://doi.org/10.1016/j.msea.2019.138607.
[10] S.M. Alimuzzaman, M.P. Jahan, C.S. Rakurty, N. Rangasamy, J. Ma, Cutting fluids in metal AM: a review of sustainability and efficiency, J. Manuf. Process. 106 (2023) 51–87, https://doi.org/10.1016/j.jmapro.2023.09.075.
[11] R. Kurz, K. Brun, Degradation in Gas Turbine Systems, in: Volume 2: Coal, Biomass and Alternative Fuels; Combustion and Fuels; Oil and Gas Applications; Cycle Innovations, American Society of Mechanical Engineers, 2000. https://doi.org/10.1115/2000-GT-0345.
[12] F. Khan, T. Miura, T. Ito, Y. Morisada, K. Ushioda, H. Fujii, Sound dissimilar linear friction welding of A7075-T6 Al and mild steel by simultaneous interfacial deformation using higher forging speed, J. Manuf. Process. 109 (2024) 512–523, https://doi.org/10.1016/j.jmapro.2023.12.023.
[13] R. Nunes, K. Faes, W. Verlinde, F. Probst, J. De Freese, J. Arnhold, W. De Waele, M. Lezaack, A. Simar, Welding of additively manufactured aluminium alloy components: challenges and mitigation strategies, Weld. World 69 (2025) 1003–1021, https://doi.org/10.1007/s40194-025-01923-9.
[14] H. White, M. Santella, E.D. Specht, Weldability of HAYNES 282 alloy for new fabrications and after service exposure, Energy Mater. 4 (2009) 84–91, https://doi.org/10.1179/174892310X12811032100114.

[15] L.O. Osoba, R.G. Ding, O.A. Ojo, Microstructural analysis of laser weld fusion zone in Haynes 282 superalloy, Mater. Charact. 65 (2012) 93–99, https://doi.org/10.1016/j.matchar.2011.12.009.
[16] L.O. Osoba, R.G. Ding, O.A. Ojo, Improved resistance to laser weld heat-affected zone microfissuring in a newly developed superalloy HAYNES 282, Metall. Mater. Trans. A 43 (2012) 4281–4295, https://doi.org/10.1007/s11661-012-1212-7.
[17] S. Singh, J. Andersson, Heat-affected-zone liquation cracking in welded cast Haynes® 282®, Metals (Basel) 10 (2019) 29, https://doi.org/10.3390/met10010029.
[18] A. Sharma, Y. Morisada, T. Nagaoka, H. Fujii, Influence of the number of FSP passes on the strength-ductility synergy of cold-rolled spark plasma sintered pure aluminum, J. Manuf. Process. 79 (2022) 296–304, https://doi.org/10.1016/j.jmapro.2022.04.061.
[19] S. Raj, P. Pankaj, P. Biswas, Friction stir welding of Inconel-718 alloy using a tungsten carbide tool, J. Mater. Eng. Perform. 31 (2022) 2086–2101, https://doi.org/10.1007/s11665-021-06331-w.
[20] M. Komarasamy, C. Smith, J. Darsell, W. Choi, S. Jana, G. Grant, Microstructure and mechanical properties of friction stir welded Haynes 282, Mater. Charact. 182 (2021) 111558, https://doi.org/10.1016/j.matchar.2021.111558.
[21] M. Komarasamy, C. Smith, J. Darsell, G. Grant, Creep behavior of friction stir processed Haynes 282, J. Mater. Eng. Perform. (2025), https://doi.org/10.1007/s11665-025-10793-7.
[22] A. Sharma, T. Miura, Y. Morisada, K. Ushioda, S. Singh, H. Fujii, Friction stir welding of Haynes 282 Ni superalloy by using a novel hemispherical tool, Sci. Rep. 14 (2024) 27826, https://doi.org/10.1038/s41598-024-79331-0.
[23] M. Mori, T. Ban, H. Takeuchi, Y. Morisada, H. Fujii, Friction Stir Welding of Thick Steel Plate Using Silicon Nitride Tool , Tetsu-To-Hagane/Journal of the Iron and Steel Institute of Japan 108 (2022) 958–965. https://doi.org/10.2355/tetsutohagane.TETSU-2022-074.
[24] A. Sharma, Y. Morisada, K. Ushioda, S. Singh, H. Fujii, Influence of welding speed on mechanical properties and fracture behaviour of friction stir welded Haynes® 282 Ni superalloy, Mater. Sci. Eng. A 941 (2025) 148619, https://doi.org/10.1016/j.msea.2025.148619.
[25] A. Sharma, Y. Morisada, H. Fujii, Bending induced mechanical exfoliation of graphene interlayers in a through thickness Al-GNP functionally graded composite fabricated via novel single-step FSP approach, Carbon N Y 186 (2022) 475–491, https://doi.org/10.1016/j.carbon.2021.10.018.
[26] D. Ambrosio, Y. Morisada, K. Ushioda, H. Fujii, Asymmetry in microstructure and mechanical properties of FSWed joints using a hemispherical tool tilted towards the retreating side, J. Manuf. Process. 119 (2024) 32–45, https://doi.org/10.1016/j.jmapro.2024.03.059.
[27] D. Ambrosio, A. Sharma, M. Mukuda, Y. Morisada, H. Fujii, Feasibility of friction stir welding using a hemispherical tool tilted towards the retreating side, J. Adv. Join. Process. 9 (2024) 100180, https://doi.org/10.1016/j.jajp.2023.100180.
[28] M. Mukuda, A. Noguchi, Y. Morisada, H. Fujii, Development of friction stir welding method using a tilted spherical tool, Sci. Technol. Weld. Join. 29 (2024) 81–88, https://doi.org/10.1177/13621718241231389.
[29] A. Sharma, T. Das, J. Paul, Performance evaluation of Al6061-graphene nanocomposites surface engineered by a novel multiple microchannel reinforcement approach in friction stir processing, Carbon Letters 31 (2021) 1111–1124, https://doi.org/10.1007/s42823-021-00230-9.
[30] A. Sharma, Y. Morisada, K. Ushioda, H. Fujii, Elucidation on the correlation between thermal stability of Al13Fe4 intermetallic phase and mechanical properties of the Al-Fe alloy fabricated via friction stir alloying, J. Alloys Compd. 967 (2023) 171732, https://doi.org/10.1016/j.jallcom.2023.171732.
[31] X. Dong, X. Zhang, K. Du, Y. Zhou, T. Jin, H. Ye, Microstructure of carbides at grain boundaries in nickel based superalloys, J. Mater. Sci. Technol. 28 (2012) 1031–1038, https://doi.org/10.1016/S1005-0302(12)60169-8.
[32] S.A. Khodir, T. Shibayanagi, Microstructure and mechanical properties of friction stir welded dissimilar aluminum joints of AA2024-T3 and AA7075-T6, in, Mater. Trans. (2007) 1928–1937, https://doi.org/10.2320/matertrans.MRA2007042.
[33] F. Khan, T. Miura, Y. Morisada, K. Ushioda, H. Fujii, Novel sacrificing-sheet linear friction welding method to fabricate sound dissimilar joint between steel and aluminum alloy, Sci. Technol. Weld. Join. 30 (2025) 273–285, https://doi.org/10.1177/13621718251353588.
[34] F. Khan, T. Miura, Y. Morisada, K. Ushioda, H. Fujii, Dissimilar joining of A7075 aluminum and SS400 steel utilizing center-driven double-sided linear friction welding using mild steel as a center material: processing, mechanical and microstructure characterization, J. Manuf. Process. 139 (2025) 67–80, https://doi.org/10.1016/j.jmapro.2025.02.017.
[35] S. Zhang, X. Lin, L. Wang, X. Yu, Y. Hu, H. Yang, L. Lei, W. Huang, Strengthening mechanisms in selective laser-melted Inconel718 superalloy, Mater. Sci. Eng. A 812 (2021) 141145, https://doi.org/10.1016/j.msea.2021.141145.
[36] X. You, Y. Tan, S. Shi, J.-M. Yang, Y. Wang, J. Li, Q. You, Effect of solution heat treatment on the precipitation behavior and strengthening mechanisms of electron beam smelted Inconel 718 superalloy, Mater. Sci. Eng. A 689 (2017) 257–268, https://doi.org/10.1016/j.msea.2017.01.093.
[37] L.A. Gypen, A. Deruyttere, Multi-component solid solution hardening, J. Mater. Sci. 12 (1977) 1034–1038, https://doi.org/10.1007/BF00540988.
[38] C. Joseph, C. Persson, M. Hörnqvist Colliander, Influence of heat treatment on the microstructure and tensile properties of Ni-base superalloy Haynes 282, Mater. Sci. Eng.: A 679 (2017) 520–530, https://doi.org/10.1016/j.msea.2016.10.048.
[39] A.J. Goodfellow, Strengthening mechanisms in polycrystalline nickel-based superalloys, Mater. Sci. Technol. 34 (2018) 1793–1808, https://doi.org/10.1080/02670836.2018.1461594.
[40] B. Liu, Y. Ding, J. Xu, Y. Gao, X. Wang, H. Zhang, Y. Hu, F. Sun, Outstanding strength-ductility synergy in Inconel 718 superalloy via laser powder bed fusion and thermomechanical treatment, Addit. Manuf. 67 (2023) 103491, https://doi.org/10.1016/j.addma.2023.103491.
[41] Y. Zhang, R.B. Sills, Strengthening via orowan looping of misfitting plate-like precipitates, J. Mech. Phys. Solids 173 (2023) 105234, https://doi.org/10.1016/j.jmps.2023.105234.
[42] F. Ichikawa, M. Sawada, Y. Kohigashi, Age-hardening behavior in γ′-phase precipitation-hardening Ni-based superalloy, ISIJ Int. 63 (2023) ISIJINT-2022-555, https://doi.org/10.2355/isijinternational.ISIJINT-2022-555.
[43] The mechanism of plastic deformation of crystals. Part I.—Theoretical, Proceedings of the Royal Society of London. Series A, Containing Papers of a Mathematical and Physical Character 145 (1934) 362–387. https://doi.org/10.1098/rspa.1934.0106.
[44] L.P. Kubin, A. Mortensen, Geometrically necessary dislocations and strain-gradient plasticity: a few critical issues, Scr. Mater. 48 (2003) 119–125, https://doi.org/10.1016/S1359-6462(02)00335-4.
[45] R. Sitek, S. Puchlerska, I. Nejman, K. Majchrowicz, Z. Pakieła, K. Żaba, J. Mizera, The Impact of plastic deformation on the microstructure and tensile strength of Haynes 282 nickel superalloy produced by DMLS and casting, Materials 15 (2022), https://doi.org/10.3390/ma15217545.
[46] Z. Islam, A.K. Agrawal, B. Rankouhi, C. Magnin, M.H. Anderson, F.E. Pfefferkorn, D.J. Thoma, A high-throughput method to define additive manufacturing process parameters: application to Haynes 282, Metall. Mater. Trans. A 53 (2022) 250–263, https://doi.org/10.1007/s11661-021-06517-w.
[47] A.S. Shaikh, E. Eriksson, M.H. Colliander, K. Minet-Lallemand, E. Hryha, Tailored heat treatments to enhance performance in additive manufactured HAYNES® 282® superalloy, Materialia (Oxf) 39 (2025) 102334, https://doi.org/10.1016/j.mtla.2025.102334.
[48] P. Maj, K. Bochenek, R. Sitek, M. Koralnik, K. Jonak, M. Wieczorek, Z. Pakieła, J. Mizera, Comparison of mechanical properties and structure of Haynes 282 consolidated via two different powder metallurgy methods: laser powder bed fusion and hot pressing, Arch. Civ. Mech. Eng. 23 (2023) 130, https://doi.org/10.1007/s43452-023-00674-y.
[49] L.F.L. Pizano, S. Sridar, R.R. De Vecchis, X. Wang, J. Biddlecom, G.J. Pataky, C. Sudbrack, W. Xiong, Recrystallization behavior and mechanical properties of Haynes 282 fabricated by wire-arc additive manufacturing with post-heat treatment, J. Manuf. Process. 119 (2024) 781–789, https://doi.org/10.1016/j.jmapro.2024.04.015.
[50] I.O. Felice, P.R. Marçal, J. Shen, L.F.L. Pizano, W. Xiong, N. Schell, T.G. Santos, J. P. Oliveira, Process development and application of hot forging arc-based additive manufacturing on Haynes® 282 for microstructural and mechanical improvements, J. Alloys Compd. 1021 (2025), https://doi.org/10.1016/j.jallcom.2025.179643.
[51] M. Zinke, S. Burger, S. Jüttner, Processing of Haynes® 282® alloy by direct energy deposition with Arc and wire, Materials 16 (2023) 1715, https://doi.org/10.3390/ma16041715.
[52] A. Deshpande, S. Deb Nath, S. Atre, K. Hsu, Effect of post processing heat treatment routes on microstructure and mechanical property evolution of Haynes 282 Ni-based superalloy fabricated with selective laser melting (SLM), Metals (Basel) 10 (2020) 629, https://doi.org/10.3390/met10050629.
[53] S. Dryepondt, M.M. Kirka, P. Fernandez-Zelaia, K.A. Unocic, Microstructure and Mechanical Properties of Haynes 282 Fabricated by Electron Beam Melting, in: J. Shingledecker, M. Takeyama (Eds.), 2019 Joint EPRI – 123HiMAT International Conference on Advances in High-Temperature Materials, ASM International, 2019: pp. 558–569. https://doi.org/10.31399/asm.cp.am-epri-2019p0558.